6-25-2010

Remote-sensing of underground caverns using a full-Maxwell's equations FDTD model

Tanner Ethan

Ethan M. Tanner
Candidate

Electrical Engineering
Department

This thesis is approved, and it is acceptable in quality and form for publication:

Approved by the Thesis Committee:

, Chairperson

REMOTE-SENSING OF UNDERGROUND CAVERNS USING A FULL-MAXWELL'S EQUATIONS FDTD MODEL

BY

ETHAN TANNER

B.S. ELECTRICAL ENGINEERING,
UNIVERSITY OF NEW MEXICO, 2008

THESIS

Submitted in Partial Fulfillment of the
Requirements for the Degree of

Master of Science, Electrical Engineering

The University of New Mexico
Albuquerque, New Mexico

May 2010

DEDICATION

I dedicate this Thesis to parents, Charles and Kathy Tanner.

ACKNOWLEDGEMENTS

I owe my deepest gratitude to my advisor Dr. Jamesina Simpson, who taught me everything I know about FDTD, and helped focus my broad interest in electrical engineering to electromagnetics. I would like to thank my wife Caitlyn and my parents Charles and Kathy who were very supportive during my collegiate studies. Furthermore, I would like to thank the numerous people who spent countless hours mentoring me during years studying engineering.

REMOTE-SENSING OF UNDERGROUND CAVERNS USING A FULL-MAXWELL'S EQUATIONS FDTD MODEL

BY

ETHAN TANNER

ABSTRACT OF THESIS

Submitted in Partial Fulfillment of the
Requirements for the Degree of

Master of Science, Electrical Engineering

The University of New Mexico
Albuquerque, New Mexico

May 2010

ABSTRACT

A need exists to reliably detect and characterize underground structures from immediately above the Earth's surface within the vicinity of the structures, as well as via aerial surveys. Sandia National Labs and the University of New Mexico have collaborated to study the feasibility of detecting and characterizing underground structures, specifically hollow rectangular-shaped caverns. This Thesis covers the computational aspects of this investigation and also focuses on the detection of caverns from immediately above the Earth's surface. Three-dimensional, full-vector Maxwell's equations finite-difference time-domain (FDTD) modeling is employed to obtain the signatures for different caverns of various depths and dimensions. It is found that by removing the signature of the ground, the presence of an underground structure is detectable.

CONTENTS

LIST OF FIGURES

LIST OF FIGURES

List of Tables

1 Introduction

A need exists to reliably detect and characterize a variety of underground caverns. The choice of remotely sensing such structures via measurement equipment located immediately above at the Earth's surface or via aerial surveys is important depending on the nature of the problem. Sandia National Laboratories and the University of New Mexico have recently collaborated to study the detection and characterization of underground structures, specifically hollow rectangular caverns using measurement equipment located immediately at the Earth's surface. This Thesis covers the computational aspects of this investigation. As part of future research, this study may be extended in a straightforward manner to the detection and characterization of caverns via aerial surveys.

In all of the computational work of this Thesis, the full-vector Maxwell's equations finite-difference time-domain (FDTD) [1] method is employed. Specifically, three-dimensional (3-D) FDTD models are generated in Fortran and parallelized using Message Passing Interface (MPI) [2]. These parallel programs are then compiled and executed on Encanto, the world's 17th fastest supercomputer as of the time of this research [3].

The Spangler Canyon Mine located at the Naval Weapons Center in China Lake, California serves as the test structure for this investigation. This mining cavern is a straight rectangular channel about four feet in width and six feet in height. One

transmitting and multiple receiving dipole reflector antennas are positioned at different points along the Earth's surface to detect and characterize this cavern.

The complete geometry of the cavern, surrounding lithosphere, and surface transmitting / receiving antennas are all modeled directly in the 3-D FDTD codes. Exploiting one of the primary advantages of computational work, numerous parametric [4] studies involving alterations of the cavern depth and dimensions as well as the positioning and orientations of the antennas may all be readily conducted using the FDTD models.

A second advantage of the computational work is that the cavern may be completely removed from the lithosphere in order to obtain the background signals. This subsequently permits extraction of specific cavern signatures via simple subtraction from the results of a model including the cavern.

The remainder of this Thesis is organized as follows. Chapter 2 provides an historical overview of remote sensing needs and capabilities and also specifies the significance of the present work. Chapter 3 describes the general FDTD method derived from Maxwell's equations, and also includes the algorithmic details of the convolutional (CPML) boundary condition utilized in all of the simulations of this Thesis. Focusing on the modeling of cavern detection, Chapter 4 introduces the FDTD grid details for the different antenna-cavern scenarios. Chapter 4 also fully describes how the antennas are implemented in

the model. Chapter 5 then presents the computational results and analyses in both the time and frequency domain. A discussion of future possibilities and applications of this research concludes the Thesis with chapter 6.

2 Background and Significance of the Present Work

From the time of James Clerk Maxwell and his contribution to classical electromagnetic theory in the 1800's, many people have studied and exploited electromagnetic phenomena. Of particular interest in this area is the detection of remote objects and structures. Starting in the 1930s, it is believed that the German Air Force used a technique to uniquely distinguish their airplanes from possible enemy aircraft at a distance beyond eyesight. Radar was used to detect the planes; however, the Germans would execute a roll with their aircraft when returning to base. This, in turn would create a distinguishing backscatter signal, identifying friend form foe aircraft [5]. Since then, much research has been conducted to develop improved remote detection capabilities.

Remote sensing techniques have advanced greatly in recent years by applying modern computational methods such as FDTD. One such example is an attempt to detect people and objects inside a building structure [6]. This particular research investigates through-the-wall sensing with the use of low-frequency, ultra-wideband radar (UWB) at a center frequency of 2.5 GHz. The computational aspect of this study provides far field radar scattering from full size rooms using complete 3-D FDTD simulations [7-10].

While [6] studies the detection of material objects, other research looks at detecting air filled spaces within a medium other than free space. For example, FDTD has been previously employed to detect a shallow tunnel surrounded by

homogeneous soil [11]. In the detection scheme of [11], the impedance change of a horizontal dipole acting as a near-field probe is calculated for when an air-filled tunnel is present versus when it is not present in the underlying ground. SEMCAD-X, a commercial FDTD software, is used for all of the simulations. A broadband voltage source over the frequency range of 50 – 250 MHz is used to detect a tunnel at a depth of 1.5 meters as well as at a depth of 2 meters. The results of [11] show that the impedance of the shallower tunnel is more than twice the value of the deeper tunnel. Further, by examining the periodic nature from the impedance deviation, the depth of the tunnel is determined.

Ground penetrating radar (GPR) is also used to detect a wide variety of subsurface structures. The need to detect landmines, archeological artifacts, geology, and pavement structures motivates the use of GPR [6]. GPR has typically involved higher frequencies for the detection of relatively shallower objects (see for example [12]), relative to the research discussed in this Thesis.

Ref [4] describes the detection of tunnels using radio frequency tomography. In that study, the GPRMAX FDTD software is employed.

Instead of detecting a hollow underground structure only from the Earth's surface, a separate method of electromagnetic cave-to-surface mapping system (ECSMS) exists [13]. In this system a loop-loop transmitter receiver configuration is used wherein the transmitter is a vertical dipole. The transmitter is placed on

the floor of the cave, which is referred to as ”ground zero” or, ”transmitter depth”. The receiver is moved over the ground at the Earth’s surface in an attempt to determine the transmitter depth. Analysis of the radiation pattern reveals that the horizontal field of the transmitter's signal passes through a null while the vertical component passes through a peak. The horizontal field peaks at a radial distance away from the transmitter at depth. When the radial distance is modeled as a circle, the depth can be determined as the diameter. The horizontal radiation pattern's null point determines the transmitter at depth. The distance between two diametrically opposite peaks of the horizontal field passing thorough the transmitter at depth reveals the depth of the transmitter. This analysis is performed for a frequency of 2.325 kHz, a cave depth of 20 meters, and a lithosphere resistivity of $100\,\Omega$.

The research described in this Thesis examines the detection of caverns in a new way relative to all of the above previous related work. For example, the tunnels of interest herein are at depths of 16.4 – 82 feet, making the near-field impedance technique of [11] not applicable. Also, relative to typical GPR investigations, lower operating frequencies are needed to detect the deeper caverns, and broadband sources are needed to in order to permit complete characterization of the caverns. And finally, of interest herein is the detection of caverns for which their existence is previously unknown. This makes the cave-to-surface mapping technique of [13] also not applicable. That is, in the work of this Thesis, the transmitting and receiving antennas are located immediately at

the Earth's surface, but above ground to prepare for the detection of caverns using aerial surveys, and operate over a general range of 50 – 220 MHz. The received power is obtained for different positions and polarizations of the receiving antennas when a tunnel is and is not present. Then the unique signature of each cavern is extracted from the received power waveforms.

3 FDTD Model Description

3.1 Introduction to FDTD

In 1966, Yee published a paper describing a numerical algorithm for solving Maxwell's curl equations on a spatial grid in the time domain [1]. Yee's algorithm is the basis for what was later termed the FDTD method [old9]. FDTD has become a popular technique for solve many science and engineering applications dealing with electromagnetic wave interactions, with about 2000 related publications appearing each year and over 30 university and commercially developed software suites available [14].

FDTD is a grid-based technique that readily provides the ability to model highly complex 3-D geometrical and material features. Also, since FDTD inherently operates in the time domain, the transient impulsive behavior is directly obtained for arbitrary time-varying sources. By applying the discrete Fourier Transform (DFT) to the computed local impulse response, the sinusoidal steady-state response may be calculated at any point in the computational domain.

To understand the basis of the FDTD algorithm, it is necessary to formulate 6 partial differential equations representing the time dependent electric and magnetic fields.

Faraday's Law:

$$\nabla X\mathbf{E} = -\frac{\partial \mathbf{B}}{\partial t} - \mathbf{M} \quad (1)$$

Ampere's Law:

$$\nabla X\mathbf{H} = \frac{\partial \mathbf{D}}{\partial t} + \mathbf{J} \quad (2)$$

where

B : magnetic flux density (webers / $meter^2$)

D : electric flux density (coulombs / $meter^2$)

M : equivalent magnetic current density (volts / $meter^2$)

J : electric current density (amperes / $meter^2$)

D and **H** can be rewritten as

D = $\varepsilon\mathbf{E} = \varepsilon_r\varepsilon_0\mathbf{E}$ (3)

$\mathbf{E} = \mu\mathbf{H} = \mu_r\mu_0\mathbf{H}$ (4)

where

ε : electrical permittivity (farads/meter)

ε_0 : free-space permittivity (8.854 $X10^{12}$ farads/meter)

ε_r : relative permittivity (dimensionless)

μ : magnetic permeability (henrys/meter)

μ_0 : free-space permeability ($4\pi X10^{-7}\, henrys/meter)$

μ_r : relative permeability (dimensionless)

J and **M** can be written as independent sources:

$J = J_{source} + \sigma E$ (5)

$$M = M_{source} + \sigma^* H \tag{6}$$

where

σ : electrical conductivity (siemens / meter)

σ^* : magnetic loss (ohms / meter)

To obtain Maxwell's curl equations (3), (4), (5), (6) are substituted into (1) and (2).

$$\frac{\partial \mathbf{H}}{\partial t} = -\frac{1}{\mu}\nabla X\mathbf{E} - \frac{1}{\mu}\left(\mathbf{M}_{source} + \sigma^*\mathbf{H}\right) \tag{7}$$

$$\frac{\partial \mathbf{E}}{\partial t} = \frac{1}{\varepsilon}\nabla X\mathbf{H} - \frac{1}{\varepsilon}\left(\mathbf{J}_{source} + \sigma\mathbf{E}\right) \tag{8}$$

Decomposing the curl equations into components yields 6 partial differential equations.

$$\frac{\partial H_x}{\partial t} = \frac{1}{\mu}\left[\frac{\partial E_y}{\partial z} - \frac{\partial E_z}{\partial y} - \left(M_{source_x} + \sigma^* H_x\right)\right] \tag{9}$$

$$\frac{\partial H_y}{\partial t} = \frac{1}{\mu}\left[\frac{\partial E_z}{\partial x} - \frac{\partial E_x}{\partial z} - \left(M_{source_y} + \sigma^* H_y\right)\right] \tag{10}$$

$$\frac{\partial H_z}{\partial t} = \frac{1}{\mu}\left[\frac{\partial E_x}{\partial y} - \frac{\partial E_y}{\partial x} - \left(M_{source_z} + \sigma^* H_z\right)\right] \tag{11}$$

$$\frac{\partial E_x}{\partial t} = \frac{1}{\varepsilon}\left[\frac{\partial H_z}{\partial y} - \frac{\partial H_y}{\partial z} - \left(J_{source_x} + \sigma E_x\right)\right] \tag{12}$$

$$\frac{\partial E_y}{\partial t} = \frac{1}{\varepsilon}\left[\frac{\partial H_x}{\partial z} - \frac{\partial H_z}{\partial x} - \left(J_{source_y} + \sigma E_y\right)\right] \tag{13}$$

$$\frac{\partial E_z}{\partial t} = \frac{1}{\varepsilon}\left[\frac{\partial H_y}{\partial x} - \frac{\partial H_x}{\partial y} - \left(J_{source_z} + \sigma E_z\right)\right] \tag{14}$$

Equations (9) – (14) are the basis of the 3-D FDTD updating equations. Yee initially applied these FDTD equations to modeling electromagnetic wave propagation in a lossless (free space) material [1]; however, FDTD has since been extended to allow modeling of electromagnetic wave interactions with materials having a variety of properties including anisotropy, dispersion, and nonlinearities.

A fundamental aspect of Yee's algorithm is that all electric and magnetic ($E_x, E_y, E_z, H_x, H_y, H_z$) components are spatially separated from each other. This may be visualized in what is called the "Yee grid cell" as seen in Figure 1.

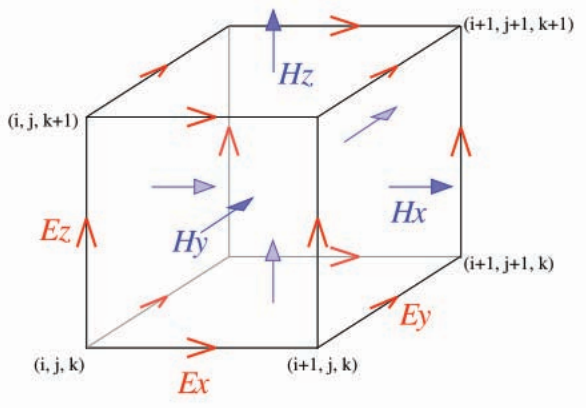

Figure 1: Yee grid cell, obtained form reference [20].

Note from Figure 1 that every **E** component is surrounded by four **H** components and every **H** component is surrounded by four **E** components. Then, not only are the fields offset in space, but they are also offset in time. That is, the Yee

algorithm takes advantage of a leapfrog updating scheme, wherein the **E** and **H** updated at alternating increments in time at each half time-step.

An entire FDTD grid is composed of multiple voxels as seen in Figure 1, which effectively creates arrays of **E** and **H** fields. All **E** updates are calculated based on the previous **E** and **H** values and are subsequently stored into memory. Then the **H** values are computed from the previous **E** and **H** values, which are then also stored in memory. The sequence continues for the **E** components using the newly acquired **H** values and previously stored **E** values. This iterative process reoccurs for the duration of the time stepping.

The following notation is used to represent space and time in the updating process. To represent the spatial increments in a three-dimensional rectangular structure the following representation is used:

$$(i, j, k) = (i\Delta x, j\Delta y, k\Delta z) \tag{15}$$

were Δx, Δy, Δz are the grid cell dimensions in the x-, y-, and z-Cartesian directions.

The function of *u* is introduced to represent a field value at a discrete point in space and time.

$$u(i\Delta x, j\Delta y, k\Delta z, n\Delta t) = u^{n}_{i,j,k} \tag{16}$$

where Δt is the time step increment.

Yee used central difference expressions with second order accuracy to describe the spatial and time derivatives of *u*.

$$\frac{\partial u}{\partial x}\left(i\Delta x, j\Delta y, k\Delta z, n\Delta t\right) = \frac{u^{n}_{i+1/2,\,j,k} - u^{n}_{i-1/2,\,j,k}}{\Delta x} + O\left[\left(\Delta x\right)^{2}\right] \tag{17}$$

$$\frac{\partial u}{\partial t}\left(i\Delta x, j\Delta y, k\Delta z, n\Delta t\right) = \frac{u^{n+1/2}_{i,j,k} - u^{n-1/2}_{i,j,k}}{\partial t} + O\left[\left(\Delta t\right)^{2}\right] \tag{18}$$

Equations (15)-(18) help provide a foundation for developing the finite-differencing updating equations used to solve Maxwell's equations spatially in three dimensions and over time. Specifically, this central differencing technique is applied to the six partial differential equations in equations (9)-(14). With a little simplification the curl equations can be rewritten in the following manner for the Ex and Hx field components:

$$E_x\Big|^{\,n+1/2}_{i,j+1/2,k+1/2} = \left(\frac{1-\dfrac{\sigma_{i,j+1/2,k+1/2}\Delta t}{2\varepsilon_{i,j+1/2,k+1/2}}}{1+\dfrac{\sigma_{i,j+1/2,k+1/2}\Delta t}{2\varepsilon_{i,j+1/2,k+1/2}}}\right) E_x\Big|^{\,n-1/2}_{i,j+1/2,k+1/2} + \left(\frac{\dfrac{\Delta t}{\varepsilon_{i,j+1/2,k+1/2}}}{1+\dfrac{\sigma_{i,j+1/2,k+1/2}\Delta t}{2\varepsilon_{i,j+1/2,k+1/2}}}\right)$$

$$\bullet\left(\frac{H_z\Big|^{\,n}_{i,j+1,k+1/2} - H_z\Big|^{\,n}_{i,j,k+1/2}}{\Delta y} - \frac{H_y\Big|^{\,n}_{i,j+1/2,k+1} - H_y\Big|^{\,n}_{i,j+1/2,k}}{\Delta z} - J_{source_x}\Big|^{\,n}_{i,j+1/2,k+1/2}\right) \tag{19}$$

$$H_x\Big|^{\,n+1}_{i-1/2,j+1,k+1} = \left(\frac{1-\dfrac{\sigma^{*}_{i,-1/2\,j+1,k+1}\Delta t}{2\mu_{i-1/2,j+1,k+1}}}{1+\dfrac{\sigma^{*}_{i-1/2,j+1,k+1}\Delta t}{2\mu_{i-1/2,j+1,k+1}}}\right) H_x\Big|^{\,n}_{i-1/2,j+1,k+1} + \left(\frac{\dfrac{\Delta t}{\mu_{i-1/2,j+1,k+1}}}{1+\dfrac{\sigma^{*}_{i-1/2,j+1,k+1}\Delta t}{2\mu_{i-1/2,j+1,k+1}}}\right)$$

$$\bullet\left(\frac{E_y\Big|^{\,n+1/2}_{i,-1/2\,j+1,k+3/2} - E_y\Big|^{\,n+1/2}_{i-1/2,j+1,k+1/2}}{\Delta z} - \frac{E_z\Big|^{\,n+1/2}_{i-1/2,j+3/2,k+1} - E_z\Big|^{\,n+1/2}_{i-1/2,j+1/2,k+1}}{\Delta y} - M_{source_x}\Big|^{\,n+1/2}_{i-1/2,j+1,k+1}\right)$$

(20)

Analogously, updating equations for the other four field components may be developed. The reader is referred to Ref [1] for these equations and for a further discussion of FDTD.

3.2 CPML

Along the outer edges of an FDTD computational domain, a non-reflective condition is needed to prevent unwanted reflections from outward propagating waves. Initially, analytical absorbing boundary conditions (ABCs) were developed to approximate a grid as though it were infinitely large. An alternative to using an ABC is to model an absorbing medium. However, early attempts to accomplish this were difficult because the boundary would only absorb incident waves normal to it.

In 1994 Berenger introduced the Perfectly Matched Layer (PML), which effectively absorbs outward propagating waves regardless of their polarization, incident angle or frequency [15]. The PML is matched at the interface between the modeling domain and the PML, and then the transmitted wave is attenuated inside of the PML layer. In this manner, PML may be used to terminate a variety of different materials, including inhomogeneous, conductive and dispersive materials [4].

After Berenger's work, a number of papers were written in an attempt to validate and improve his original PML algorithm. The most notable is the development in

2000 of the Convolution Perfectly Matched layer (CPML) [4]. CPML employs an extended form of Maxwell's equations. This form uses stretched coordinates, where Maxwell's equations are modified as $(e^{j\omega t})$, which can be rewritten in the following manner.

$$\nabla_e X\mathbf{E} = -j\omega\mu\mathbf{H} - \mathbf{M} \tag{21}$$

$$\nabla_h X\mathbf{H} = j\omega\varepsilon\mathbf{E} + \mathbf{J} \tag{22}$$

$$\nabla_h \cdot \mathbf{J} + j\omega\rho = 0 \tag{23}$$

$$\nabla_e \cdot \mathbf{M} + j\omega\rho^* = 0 \tag{24}$$

where

$$\nabla_e = \hat{x}\frac{1}{e_x}\frac{\partial}{\partial x} + \hat{y}\frac{1}{e_y}\frac{\partial}{\partial y} + \hat{z}\frac{1}{e_z}\frac{\partial}{\partial z} \tag{25}$$

$$\nabla_h = \hat{x}\frac{1}{h_x}\frac{\partial}{\partial x} + \hat{y}\frac{1}{h_y}\frac{\partial}{\partial y} + \hat{z}\frac{1}{h_z}\frac{\partial}{\partial z} \tag{26}$$

Given an interface between two mediums that is normal to the z-axis, the phase matching condition can be described in the following way.

$$k_{x1} = k_{x2} \tag{27}$$

$$k_{y1} = k_{y2} \tag{28}$$

Consider the situation where $e_x = h_x, e_y = h_y, e_z = h_z$, the permittivity and permeability are equal, $\varepsilon_1 = \varepsilon_2, \mu_1 = \mu_2$, and the wave impedance is the same for both mediums. To create an environment where reflection does not exist for arbitrary angles of incidence and frequency between two perfectly matched mediums, let $e_{x1} = e_{x2}$, $e_{y1} = e_{y2}$.

The requirements for the PML are:

$$e_{xi} = h_{xi},\ e_{yi} = h_{yi},\ e_{zi} = h_{zi},\ \text{(i=1,2)} \tag{29}$$

$$\varepsilon_1 = \varepsilon_2, \mu_1 = \mu_2 \tag{30}$$

$$s_x = e_{x1} = e_{x2},\ s_{y=} e_{y1} = e_{y2} \tag{31}$$

which yields the results:

$$\theta_1 = \theta_2,\ \varphi_1 = \varphi_2 \tag{32}$$

$$\Gamma = 0,\ \text{(0=TE or TM)} \tag{34}$$

Some of the variables can be adjusted $\left(e_{z2} = s_2\right)$ to be an arbitrary number or function, where the waves in the PML can be attenuated by the imaginary part of $s_2 : \mathrm{Im}\left[s_2\right]$, where $s_2 : \mathrm{Re}\left[s_2\right] + j\,\mathrm{Im}\left[s_2\right]$. With these requirements, the propagation constant in the host medium (index 1) and the PML medium (index 2) can be written as shown.

$$k_{x1} = k_{x2} = k_1 \sin\theta_1 \cos\varphi_1 \tag{35}$$

$$k_{y1} = k_{y2} = k_1 \sin\theta_1 \cos\varphi_1 \tag{36}$$

$$k_{z1} = k_1 \cos\theta \tag{37}$$

$$k_{z2} = s_2 k_1 \cos\theta \tag{38}$$

where

$$k_1^2 = \omega^2 \varepsilon_1 \mu_1 \tag{39}$$

The coordinate-stretched form of Maxwell's equations used in the PML in frequency domain can be written as follows.

$$\left(\hat{x}\frac{1}{s_x}\frac{\partial}{\partial x} + \hat{y}\frac{1}{s_y}\frac{\partial}{\partial y} + \hat{z}\frac{1}{s_z}\frac{\partial}{\partial z}\right) X\mathbf{E} = -j\omega\mu\mathbf{H} - \mathbf{M} \tag{40}$$

$$\left(\hat{x}\frac{1}{s_x}\frac{\partial}{\partial x}+\hat{y}\frac{1}{s_y}\frac{\partial}{\partial y}+\hat{z}\frac{1}{s_z}\frac{\partial}{\partial z}\right)X\mathbf{H}=j\omega\varepsilon\mathbf{E}+\mathbf{J} \tag{41}$$

$$\left(\hat{x}\frac{1}{s_x}\frac{\partial}{\partial x}+\hat{y}\frac{1}{s_y}\frac{\partial}{\partial y}+\hat{z}\frac{1}{s_z}\frac{\partial}{\partial z}\right)\cdot\mathbf{J}+j\omega\rho=0 \tag{42}$$

$$\left(\hat{x}\frac{1}{s_x}\frac{\partial}{\partial x}+\hat{y}\frac{1}{s_y}\frac{\partial}{\partial y}+\hat{z}\frac{1}{s_z}\frac{\partial}{\partial z}\right)\cdot\mathbf{M}+j\omega\rho^{*}=0 \tag{43}$$

Berenger proposed stretched-coordinates wherein

$$s_i=1+\frac{\sigma_i}{j\omega\varepsilon_0},\quad \text{(i = x, y, or z) [4]} \tag{44}$$

Using Berenger's PML, it is easy to implement the stretched from (s_i). One can get back to the extended form of Maxwell's equations by taking the inverse Laplace transform and performing convolution. Despite the robust nature of the PML it still has disadvantages in its applications. The PML is ineffective at absorbing evanescent waves [16-18]. Furthermore, comparatively to the CPML, it is computationally more intensive taking four times the amount of memory for its formulation [4]. Noting some of the limitations of the already efficient PML, the CPML is able to compensate for these inadequacies and results in less reflection from the incident wave.

For the CPML, s_i is adjusted to:

$$s_i=k_i+\frac{\sigma_i}{\alpha_i+j\omega\varepsilon_0},\quad \text{(i = x ,y, or z) [4]} \tag{45}$$

where α_i,σ_i,k_i are all positive real numbers. Similar to the PML, for the CPML, one can perform derivations on s_i to get back to the extended from of Maxwell's

equations using the same method; however it is more difficult. Aside from the numerical description of how the CPML works, an actual implementation in the form of a plot helps validate the theory. Figure 2 depicts a visual representation of how the CPML lies on the edge of the computational domain and absorbs the energy of an impinging wave.

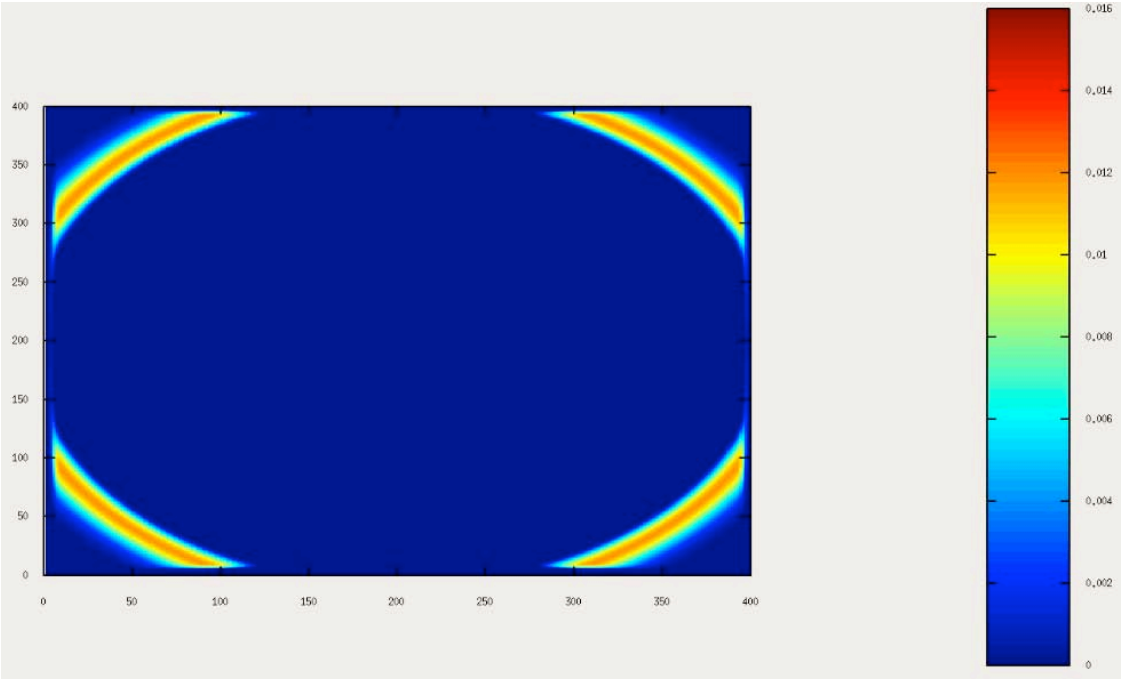

Figure 2: Two-Dimensional FDTD model having CPML boundary conditions, created by the author.

The source of the wave originates from the center of the diagram and propagates outward towards the boundary of the FDTD lattice. If the CPML were not implemented, reflection would occur and the wave would no longer appear circular.

4 Modeling Cases

In this Section, the FDTD models used to simulate the detection of underground caverns are described. Each simulation employs five total corner reflector dipole antennas as illustrated in Fig. 3. Of the five total antennas employed in each simulation, one is transmitting and four are receiving. In Section 4.1, the implementation of the resistive voltage source used to excite the transmitting dipole corner reflector antennas is provided. In Section 4.2, the receivers are described. Finally, Section 4.3 describes the different simulation cases.

Figure 3 shows a representation of what was modeled for the antennas. The blank area at the center of the two sides of the dipole (between the dotted lines) is where the source / receiving resistor is modeled.

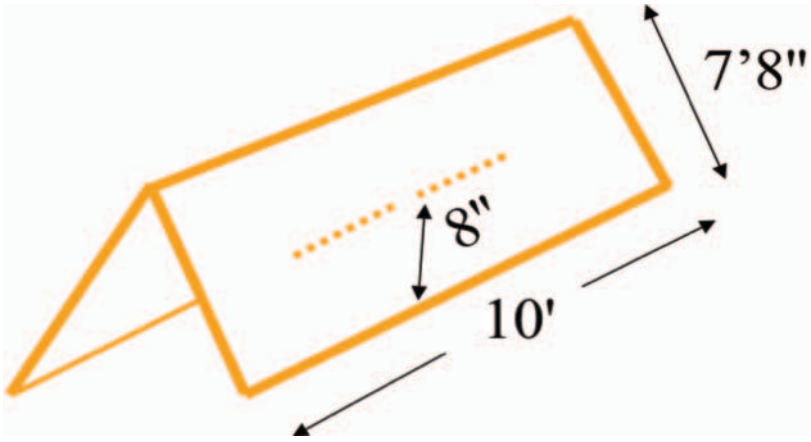

Figure 3: Representation of the modeled dipole antenna with mesh corner

reflector.

4.1 Transmitter Resistive Voltage Source

FDTD has the capability to model lumped circuit elements including a nonreflecting resistive voltage source. This is the type of source used to excite the transmitting corner reflector dipole antenna in the research of this Thesis. The source lies on a y-directed lumped element with a $50\,\Omega$ impedance. The source is a Gaussian modulating a sinusoid as follows:

$$Source = \sin(2.0 \cdot \pi \cdot (n - n_0) \cdot 106 \text{å} MHz \cdot \Delta t) \cdot e^{\left(-\left(\frac{n-n_0}{n_{half}}\right)^2\right)} \quad (46)$$

where n_o *is the time step at which the source waveform is centered in time, and* n_{half} is the half width of the Gaussian. At the location of the resistive voltage source, the $\mathbf{E}_y$ component is excited as follows:

$$\mathbf{E}_y\Big|_{i,j,k}^{n+1} = R_{1s} \cdot E_y\Big|_{i,j,k}^{n+1} + R_{2s} + (\nabla XH)_y\Big|_{i,j,k}^{n+1/2} + R_{3s} \cdot Source\Big|^{n+1/2} \quad (47)$$

The variables R_{1s}, R_{2s}, R_{3s} are modified updating coefficients for the E-field at the location of the resistive voltage source. These values are calculated before time stepping begins:

$$R_{1s} = \frac{1 - \dfrac{\Delta t \cdot \Delta z}{2 \cdot R_s \cdot \varepsilon_0 \cdot \Delta x \cdot \Delta y}}{1 + \dfrac{\Delta t \cdot \Delta z}{2 \cdot R_s \cdot \varepsilon_0 \cdot \Delta x \cdot \Delta z}} \quad (48)$$

$$R_{2s} = \frac{\dfrac{\Delta t}{\varepsilon_0}}{1 + \dfrac{\Delta t \cdot \Delta z}{2 \cdot R_s \cdot \varepsilon_0 \cdot \Delta x \cdot \Delta z}} \quad (49)$$

$$R_{3s} = \frac{\dfrac{\Delta t}{R_s \cdot \varepsilon_0 \cdot \Delta x \cdot \Delta y}}{1 + \dfrac{\Delta t \cdot \Delta z}{2 \cdot R_s \cdot \varepsilon_0 \cdot \Delta x \cdot \Delta z}} \tag{50}$$

where the value of the resistor is $R_s = 50\Omega$.

Nine separate frequency ranges ("bins") are considered over the frequency range of 54 – 220 MHz as listed in Table 1 below. In this Thesis, computational results for bins 5 and 8 will be provided. The center frequency of the source corresponds to the center frequency of the selected bin. The source spectrum then also extends with sufficient power over the full spectral width of the corresponding bin. Also depending on the selected bin, the length of the transmitter (and receiver) dipoles are chosen according to the last column of Table 1. The transmitters (and later receivers) are then completed by modeling each dipole and reflector as having the conductivity of copper, $\sigma = 5.8 X 10^7 \frac{S}{m}$.

The nine total bins are as follows:

Table 1: List of bins with their associated frequency and antenna length.

Bin Number	Starting Frequency (MHz)	Ending Frequency (MHz)	Dipole ½ Length (Inches)
1	54	63	47
2	66	76	40
3	76	88	33
4	89	102	28
5	98	114	24 ¼
6	116	156	21
7	152	171	18
8	167	194	16
9	191	220	13

4.2 Receiver Resistors

All of the FDTD models employ four dipole antenna receivers having corner mesh reflectors. The corner mesh reflectors and dipoles have a thickness of one grid cell. From the ground, the corner mesh reflectors form an inverted-V with the apex reaching a height of 5 feet 6 inches. The horizontal dipole of the antennas are centered under the corner reflector at a height of 8 inches above the ground.

At the center of the dipole is a $50\,\Omega$ resistor over which the received voltage is recorded. The length of the receiver dipoles are also chosen according to Table 1 and the selected bin for the simulation. And finally, the receiver dipoles and corner reflectors are of conductivity, $\sigma = 5.8X10^{7}\frac{S}{m}$.

The finite-difference representation of the curl equations as shown in equation (19) contain values that are used as the updating coefficients and are denoted as C_a and C_b. Once the material parameters are determined, these updating coefficients are utilized to model the antennas and ground.

$$C_a\Big|_{i,j,k} = \left(\frac{1-\frac{\sigma_{i,j,k}\Delta t}{2\varepsilon_{i,j,k}}}{1+\frac{\sigma_{i,j,k}\Delta t}{2\varepsilon_{i,j,k}}}\right) \tag{51}$$

$$C_b\Big|_{i,j,k} = \left(\frac{\frac{\Delta t}{\varepsilon_{i,j,k}}}{1+\frac{\sigma_{i,j,k}\Delta t}{2\varepsilon_{i,j,k}}}\right) \tag{52}$$

The three-dimensional positioning of the antennas inside of the computational mesh is pre-determined. Programmatic if-statements and loops are developed to ensure that the updating coefficients with values pertinent to describing the antenna are incorporated into the FDTD grid. It is important to note however, C_a and C_b are used in describing the antenna and mesh, but other coefficients are used to define the center of the dipole (resistor location). As mentioned previously, for the one cell at the center of the antenna modified updating coefficients are employed. In this case the values for R_{1s} and R_{2s} in equations

(48) and (49) are analogous to the coefficients C_a and C_b.

4.3 Simulation Cases

The simulations conducted for this research encompass several different scenarios. As mentioned previously, the model in this Thesis uses a three-dimensional grid with uniform spatial increments in each Cartesian direction ($\Delta x = \Delta y = \Delta z = 0.118$ inches). The entire grid contains over 949 million individual cells with a time increment (Δt) set to 4 psec.

Two different arrangements of the antenna positions are modeled in the FDTD grid and used in the detection of the underlying cavern. These two arrangements are illustrated in Figures 4 and 5 below. In addition to these two arrangements of the antennas, two polarizations of the antennas are simulated in separate modeling cases: parallel and cross polarization. The polarization only describes the physical orientation of the dipole and reflector as being aligned parallel to the underlying cavern or perpendicular (cross polarization).

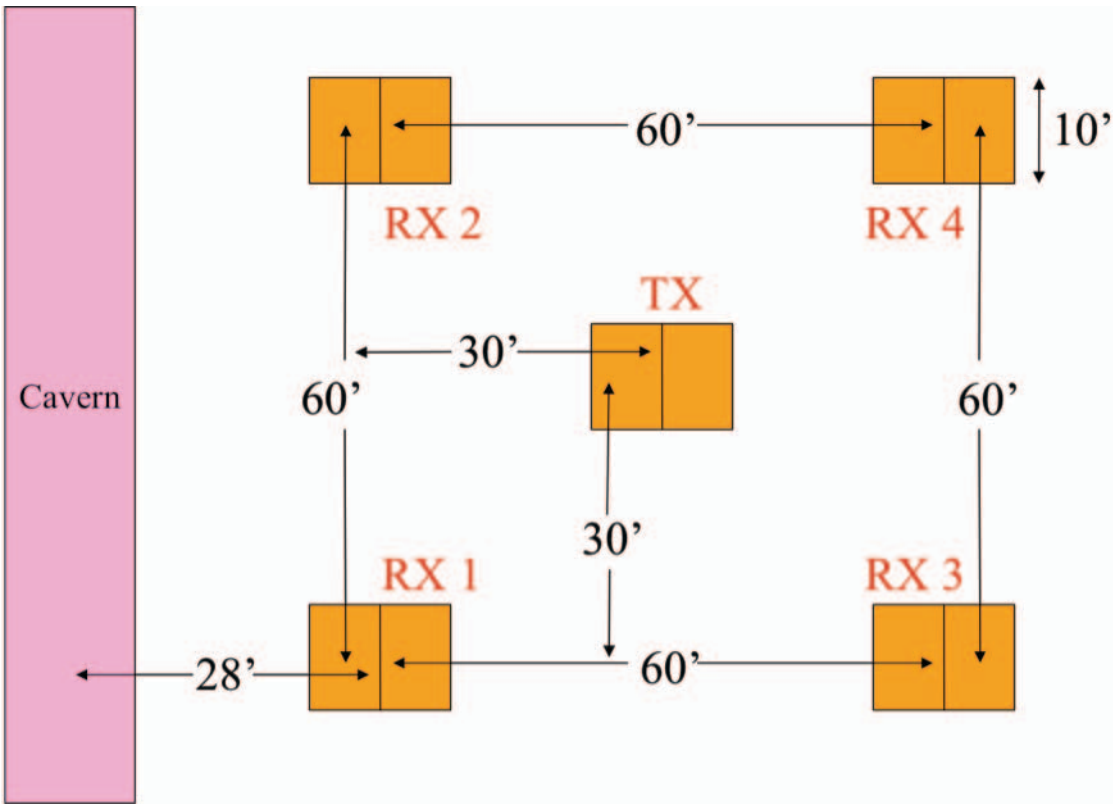

Figure 4: Plan view of Position 1, parallel polarization.

Figure 4 shows the parallel polarization case for the first arrangement of the antennas, wherein the cavern is positioned to the left of the antennas. In this situation the four receiving antennas are separated 60 feet apart, which translates to 610 grid cells. The receiving antennas are positioned so that they form a square, with the transmitting antenna located directly in the center, equidistant to all other antennas.

The second arrangement has the same configuration of the antennas; however all five antennas are shifted so that the transmitting antenna is positioned directly over the cavern. This situation can be viewed for the parallel polarization as

shown in Figure 5 below.

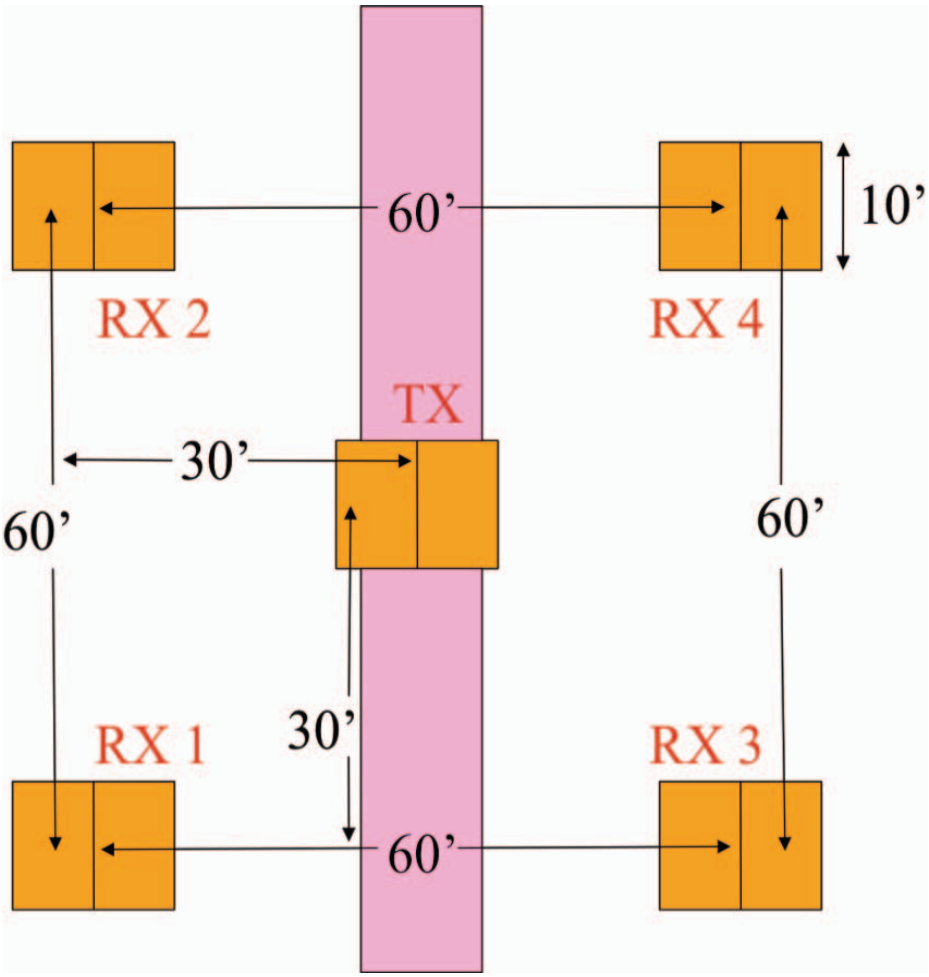

Figure 5: Plan view of Position 2, parallel polarization.

A third arrangement could be considered, wherein the antennas are all located to the left side of the tunnel instead of the right side. However, due to grid symmetry in the computations, these simulations would provide the same result as for Position 1 above.

Running multiple simulations wherein the position of the transmitting antenna is shifted in space relative to the cavern, allows for an incident wave on the cavern

at multiple angles. These simulation results thus have application to aerial surveys wherein the transmitting antenna is mounted on a moving aircraft and generates a wave incident on the cavern at varying angles.

To provide enough space to model the tunnel, antennas and the CPML, the (i) direction extend for 1304 cells while (j) direction extend for 1040 cells.

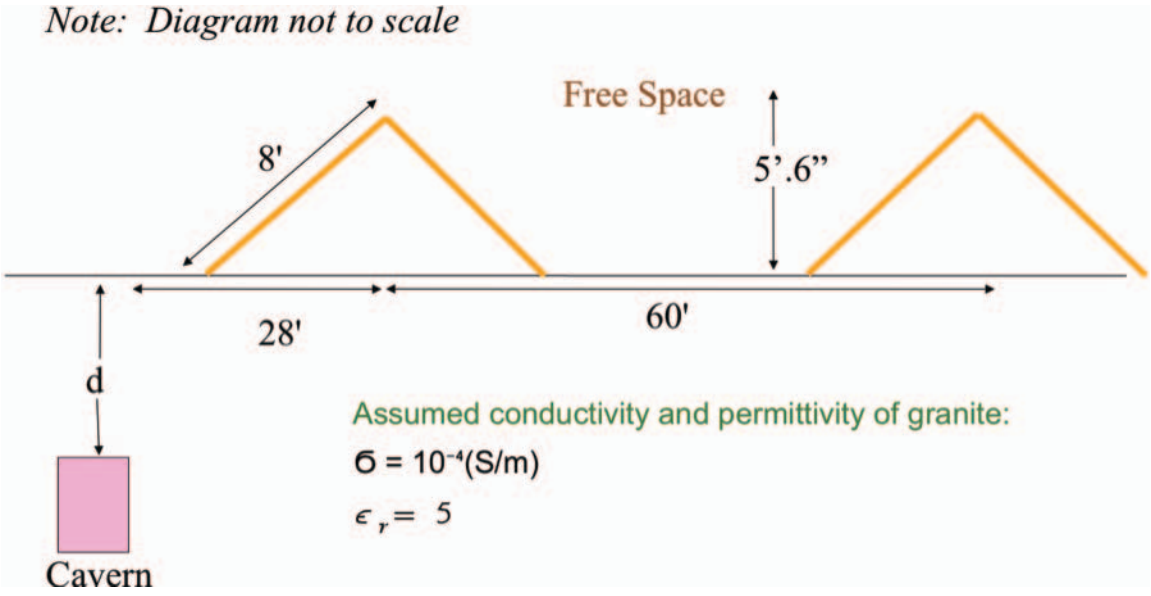

Figure 6: Side view of Position 1, parallel polarization case.

As Fig. 6 illustrates, the area above the ground is modeled as free space. Physical measurements taken in the area around the Spangler Canyon Mine indicate that the ground is comprised largely of granite [19]. The granite is assumed to have a conductivity and relative permittivity of $\sigma = 10^{-4}\frac{S}{m}, \varepsilon_r = 5$, respectively, in the FDTD model [7 – 8]. Two different depths of the cavern are considered in the FDTD model: a depth of 16.4 feet and a depth of 82 feet. In

order to replicate the Spangler Canyon Mine tunnel, the nominal width of the cavern is 4 feet and its height is 6 feet. However, a second tunnel is simulated for comparison having a width of 8 feet and a height of 6 feet. Lastly, the tunnel is assumed infinitely long in the FDTD simulations.

5 Results

The modeling results for the various simulation cases are now provided. Since FDTD operates in the time domain, the received time waveforms are shown first in Section 5.1. Then, by applying a DFT to the time domain results, the corresponding spectra for the time-waveforms of Section 5.1 are obtained and shown in Section 5.2.

5.1 Time-Domain Results

Recall Table1, which lists the 9 frequency bins. The following graphs show results for bin 5 at 98 – 114 MHz and for bin 8 using a smaller dipole and at 167 – 194 MHz. Simulations for the two arrangements of the antennas are indicated as Position 1 and Position 2. Furthermore, the received waveforms for the individual antennas are labeled as channels. Channel 1, Channel 2 analogously relate to RX1, RX 2, which vary spatially only in the (j) direction.

Starting with the first Position where the antennas lie on the earth's surface to the right of the cavern (Position 1), the signature of the underground structure is obtained. Due to symmetry, for Position 1, the results from Channel 1 and Channel 2 yield the same results; the same is true for Chanel 3 and Channel 4. For this reason, only the results acquired for Channel 1 and Channel 3 are displayed. The majority of the simulations evaluate the case of the antennas for parallel polarization; a few samples of cross polarization are provided for comparison.

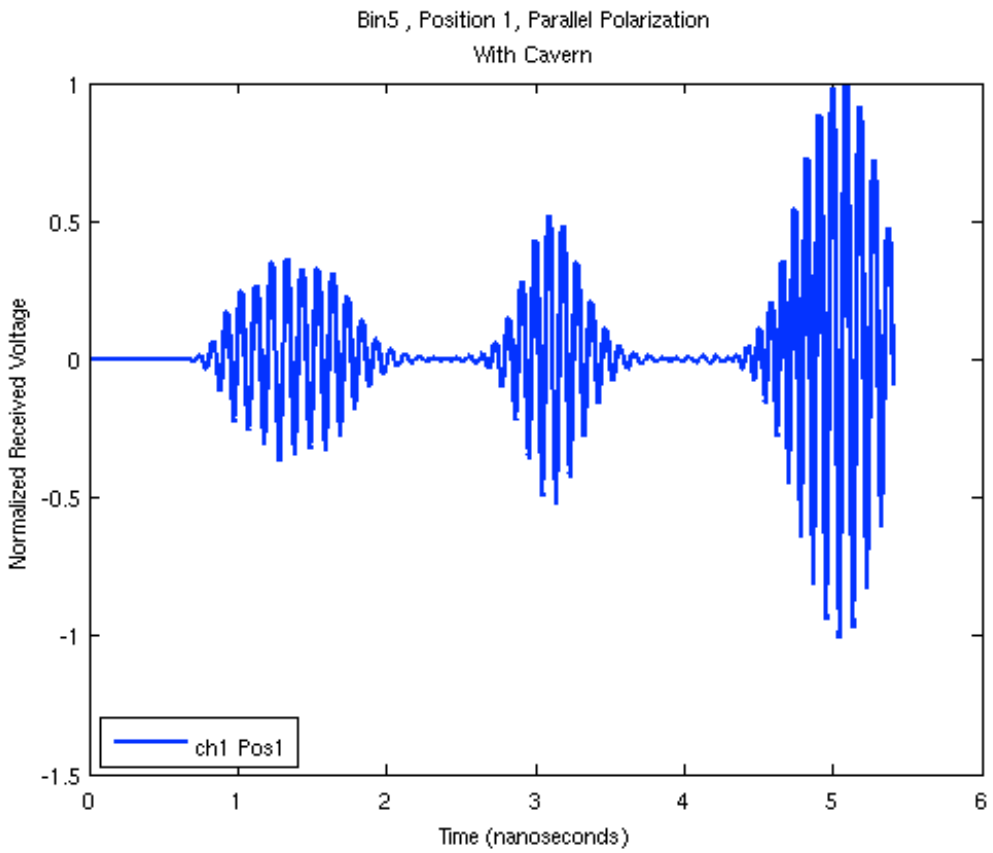

Figure 7: Received time waveform of channel 1 for Position 1 and Bin 5 when the cavern is present.

The initial pulse at about 1.4 nanoseconds in Figure 7, represents the direct wave from the source antenna to the receiver. A small time delay is observable before the second pulse occurs at about 3 nanoseconds, which is the initial reflection from the cavern. Another simulation is performed over the ground without a cavern present. Figure 8 show the background signature, which is needed to obtain the cavern signature.

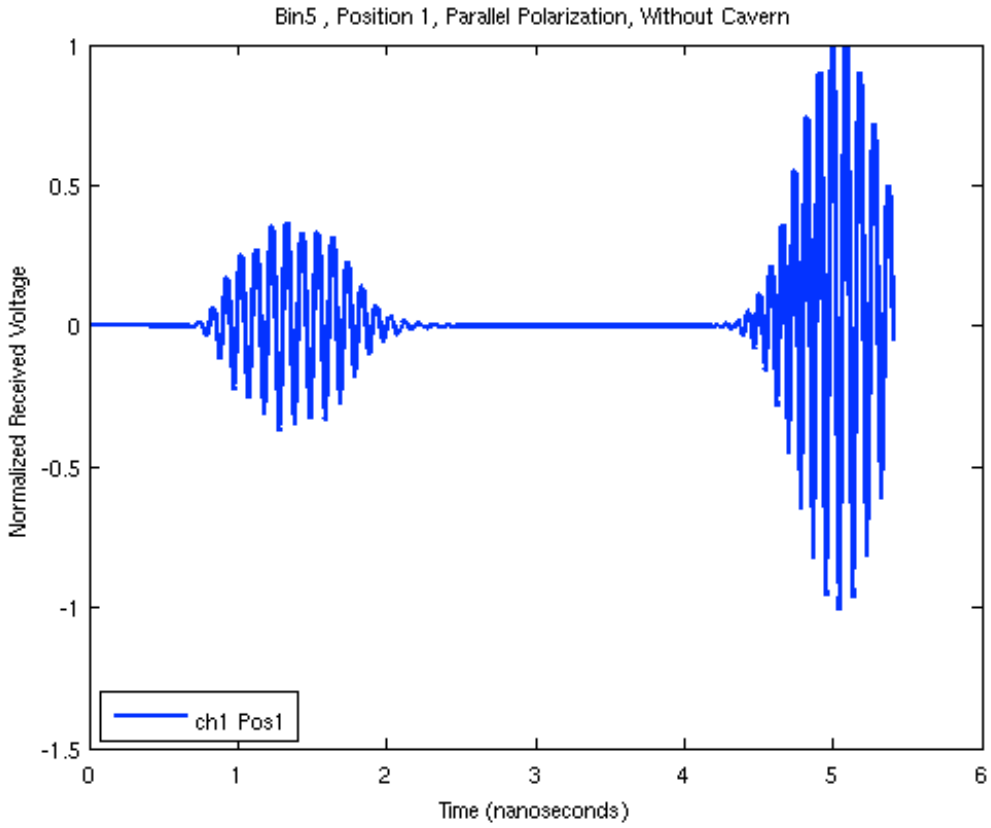

Figure 8: Received time waveform of channel 1 for Position 1 and Bin 5 when the cavern is not present.

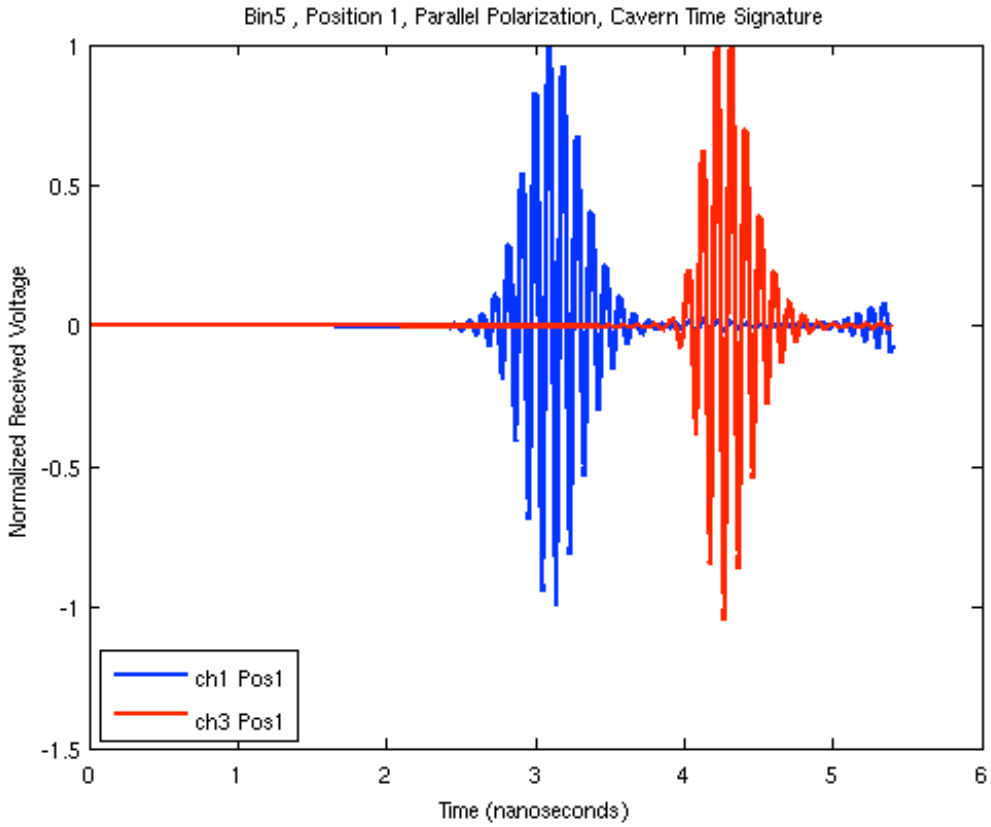

Figure 9: Time-domain signature of the cavern from Position 1 (obtained by subtracting the results of Figure 8 from Figure 7).

Using the results shown in Figure 7 and Figure 8, the signature of purely the cavern is obtained by a simple subtraction. Figure 9 includes the signature of the cavern received by antennas one and three. As seen in Figure 4, Antenna 1 is located closer to the cave than Antenna 3. This correlation can be noticed in Figure 9 by observing the time delay between the two antennas.

For Position 2 results, the received signals when the antennas are positioned symmetrically over the cave, see Figure 2.

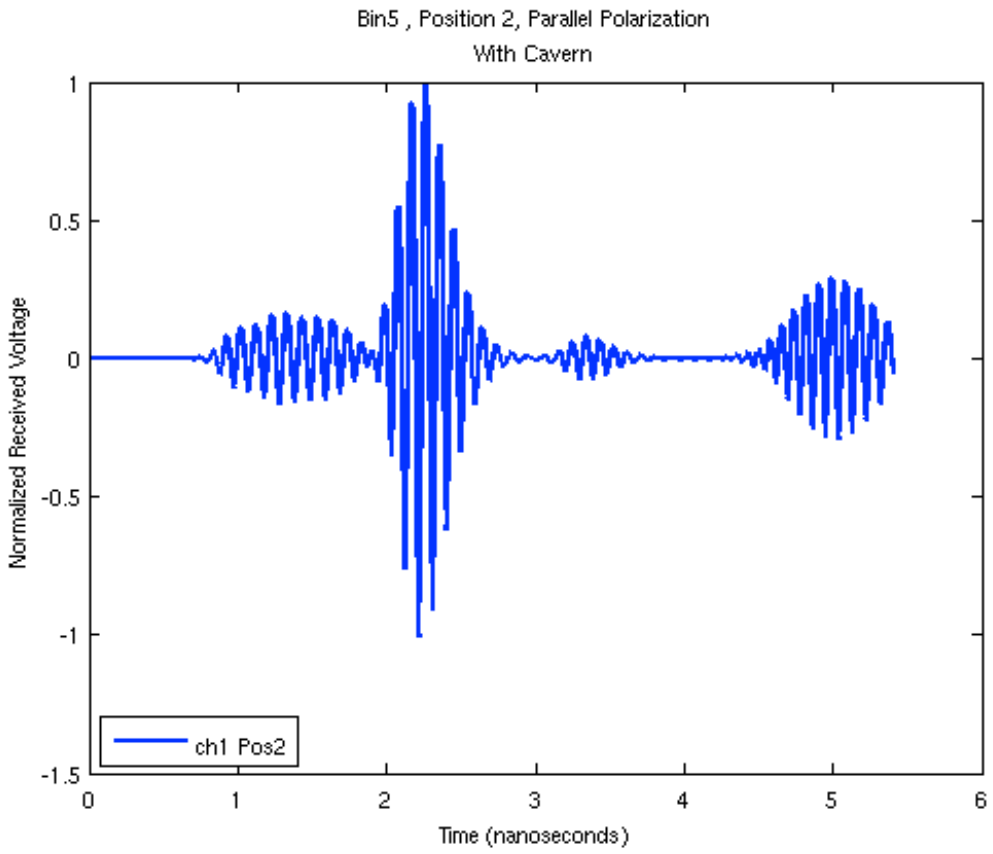

Figure 10: Received time waveform of channel 1 for Position 2 and Bin 5 when the cavern is present.

The above figure displays the received signal of both the cavern and the ground. Below Figure 11 shows the signature of only the ground. Since the spatial distance between all four receiving antennas and the cavern are identical, the received signals are all identical.

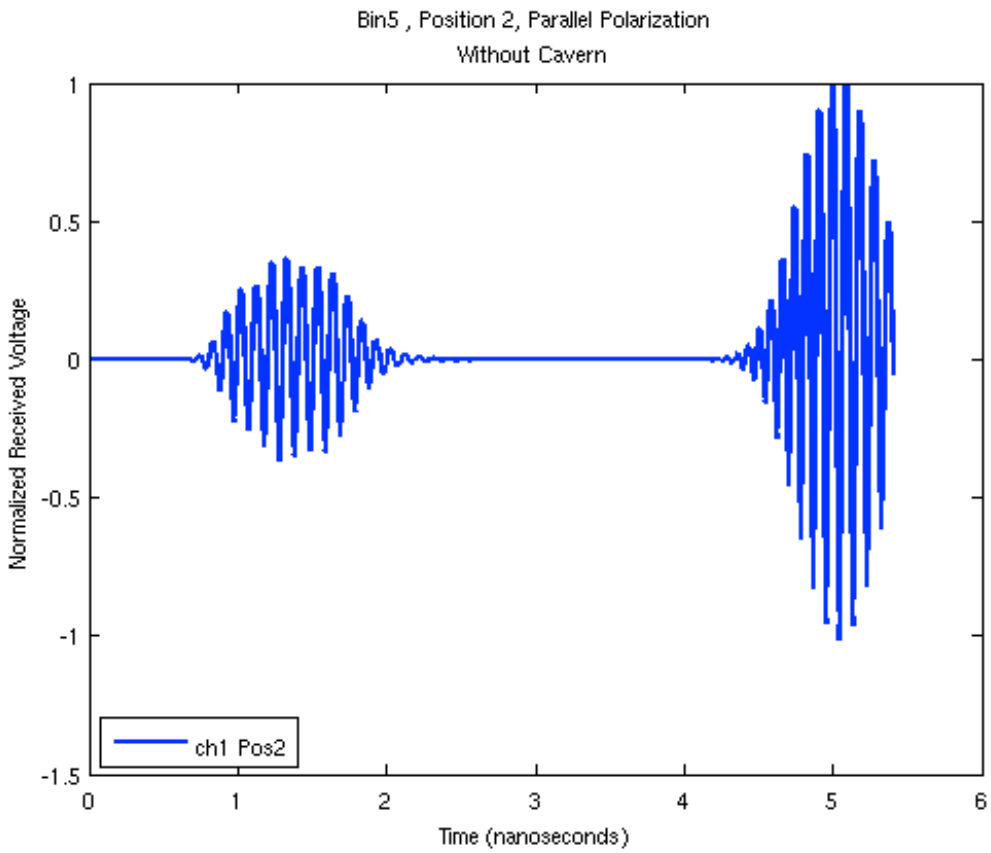

Figure 11: Received time waveform of channel 1 for Position 2 when the cavern is not present.

The below figure does validate the proposed symmetrical physical positioning of the antennas. Figure 12 displays the signature of the cavern with the ground subtracted. Notice how the red line from Channel 3 masks the signature of Channel 1.

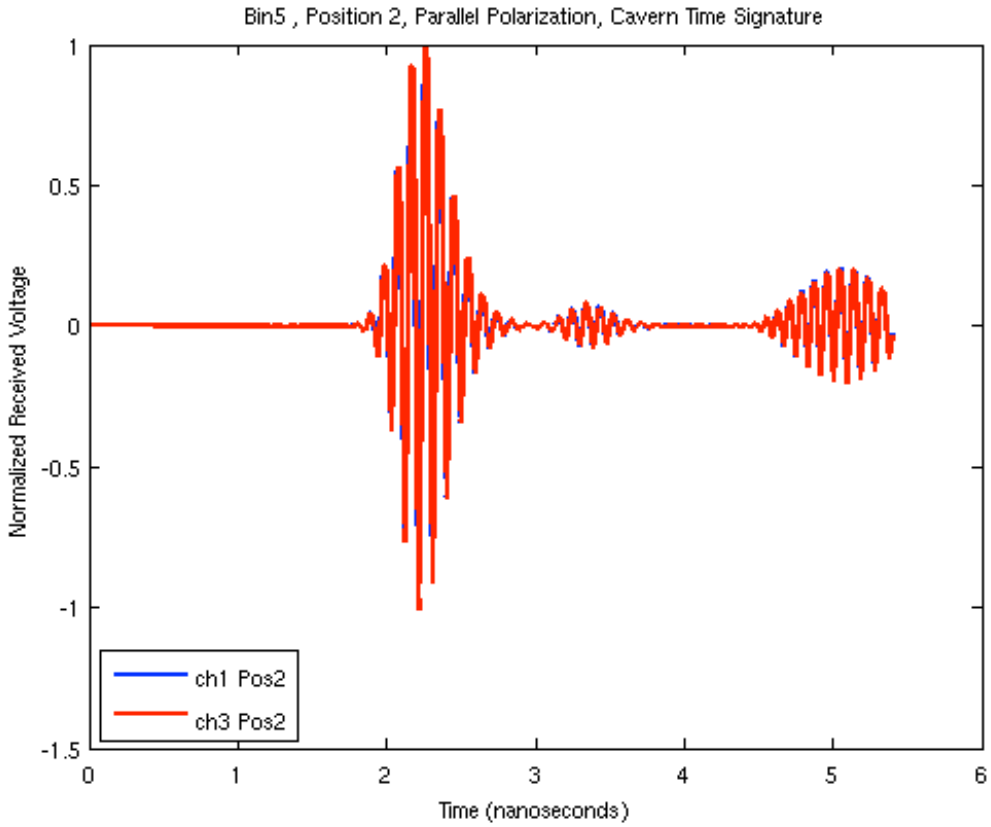

Figure 12: Time-domain signature of the cavern for Position 2 and Bin 5

The above figures were acquired from bin 5, the set of data with a frequency spectrum of 98 – 114 MHz. A shorter dipole is used to obtain the signatures for the following figures, using bin 8, 167 – 194 Mhz. The below figure displays the signature of the cavern acquired from an antenna with a parallel polarization.

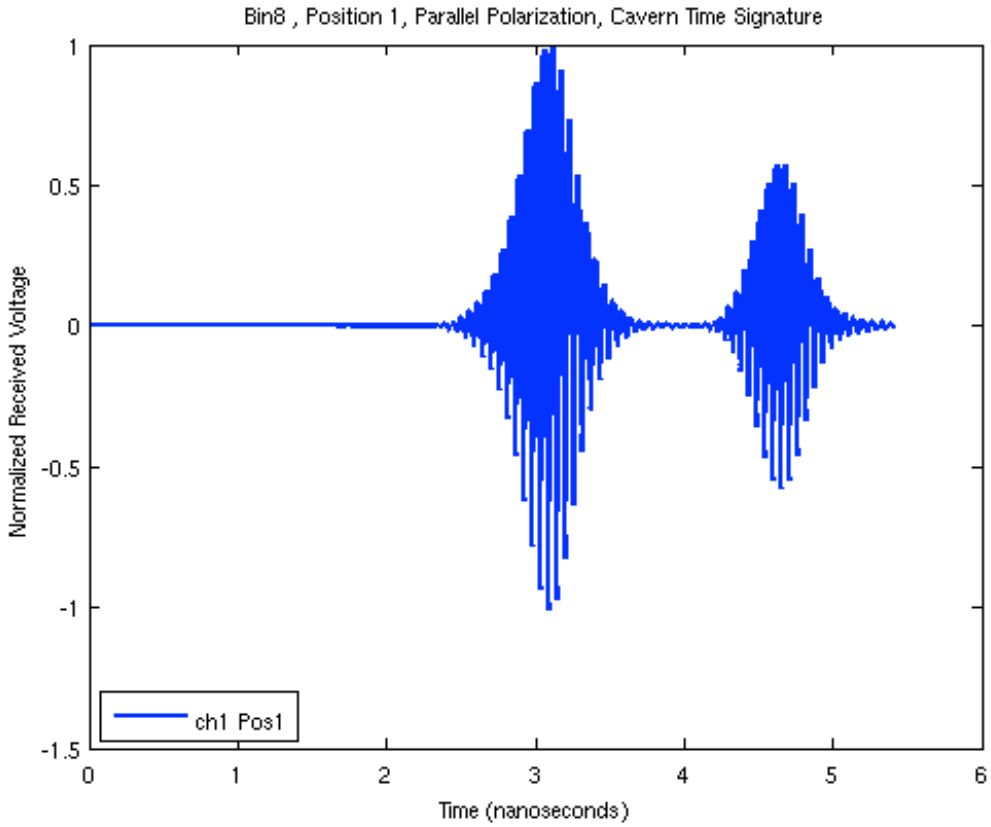

Figure 13: Time-domain signature of the cavern for Position 1 and Bin 8.

With an understanding of the significance of the time-domain plots, the remaining configurations including cross polarization, a shallow cavern and a cavern with a different shape are shown below.

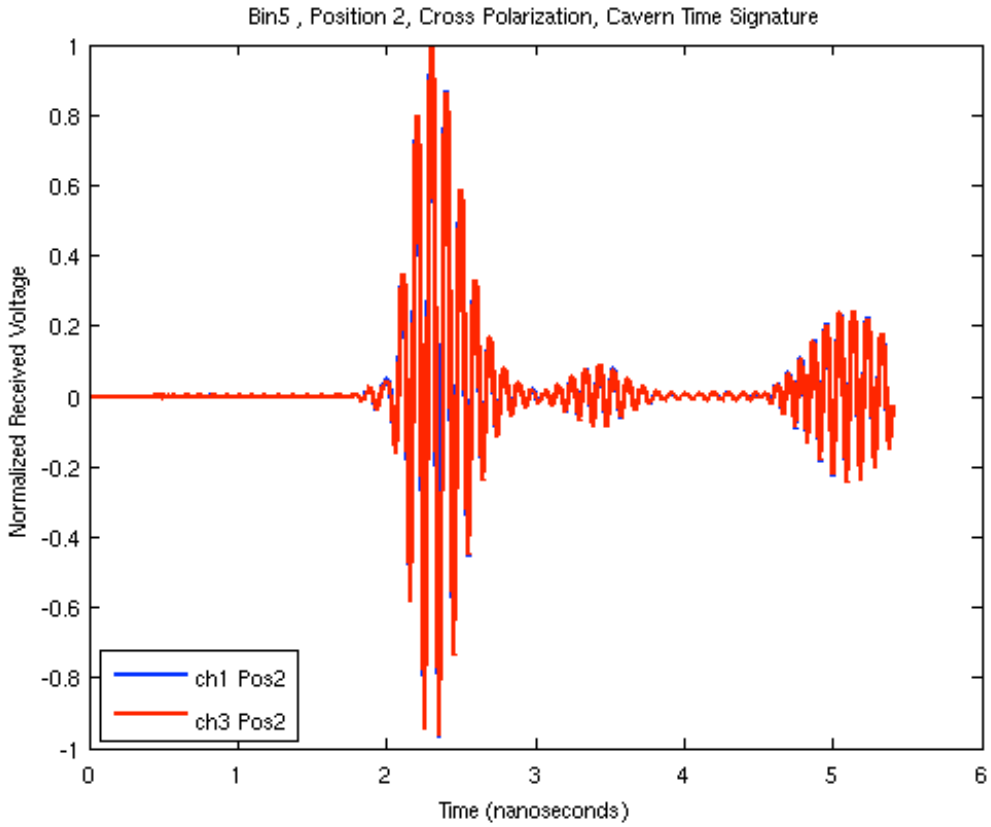

Figure 14: Time-domain signature of the cavern for Position 2, Bin 5, and for cross polarization

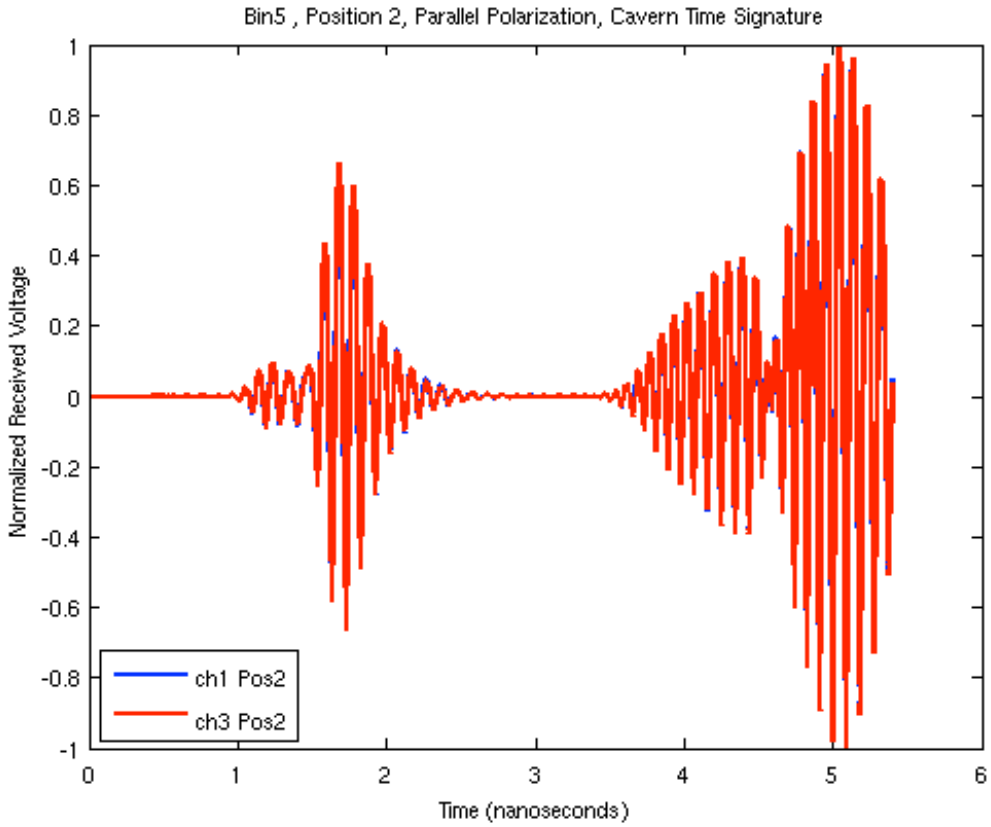

Figure 15: Time-domain signature of the cavern for Position 2, Bin 5, and for a cavern of depth 16.404 feet.

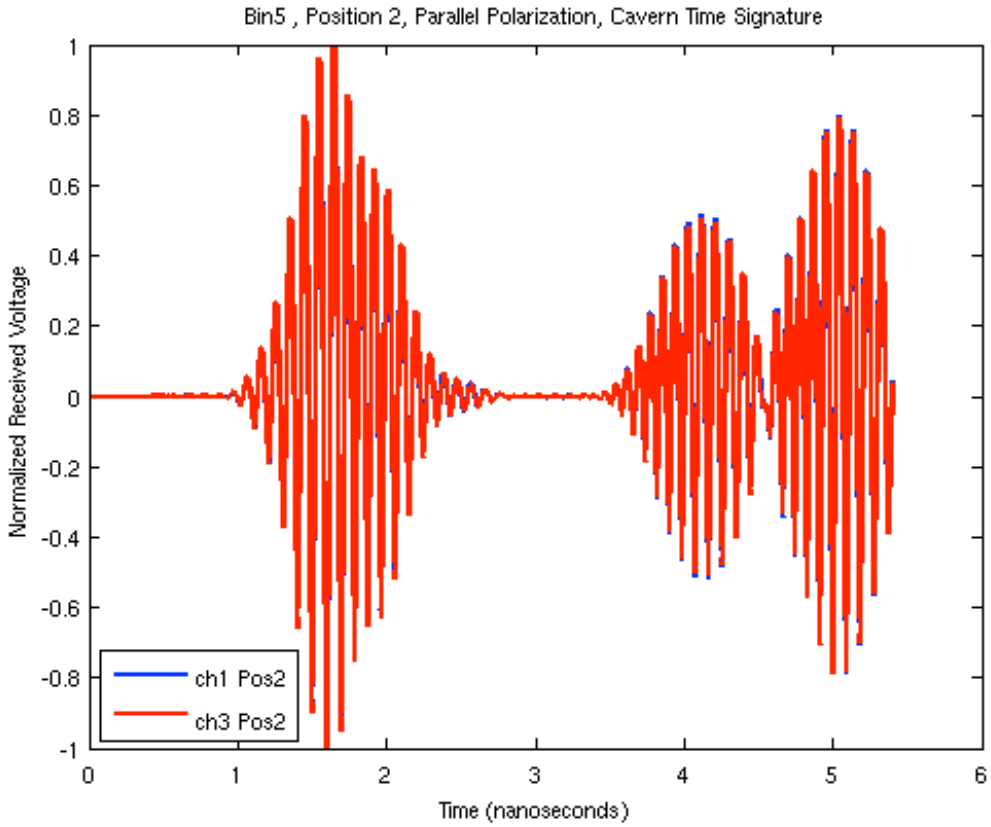

Figure 16: Time-domain signature of the cavern for Position 2, Bin 5, Cavern of depth of 16.404 feet and having dimensions of 8 feet by 6 feet.

5.2 Frequency-Domain Results

Once a DFT is applied to the time signatures, the frequency response is found. The normalized received power for the cavern signature for Positions 1 and 2 and for bin 5 and bin 8 are first obtained. The remaining waveforms were all produced using the entire time-domain signature of 135,000 time steps.

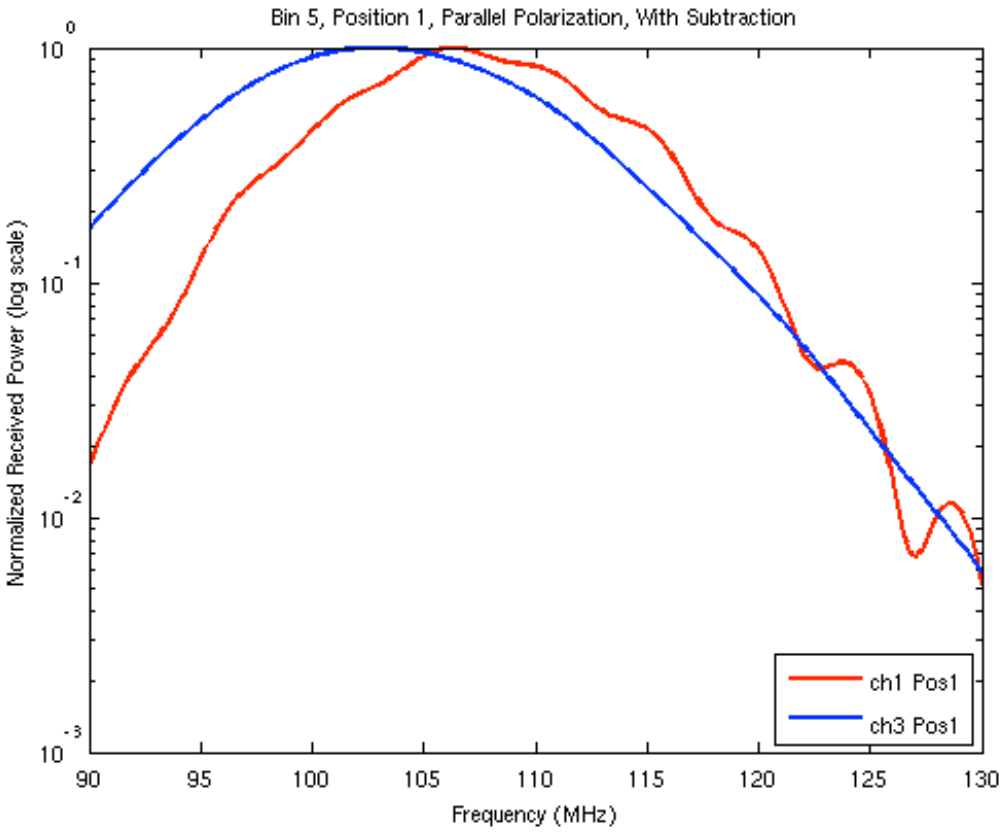

Figure 17: Frequency-domain signature of the cavern for Position 1 and for Bin 5 (corresponding to Figure 9).

Notice that the peaks in Figure 17 are not as recognizable as in the following figures. Channel 1 displays peaks approximately every 4.75 MHz, but channel 3

is too far away from the cavern to obtain a cavern signature.

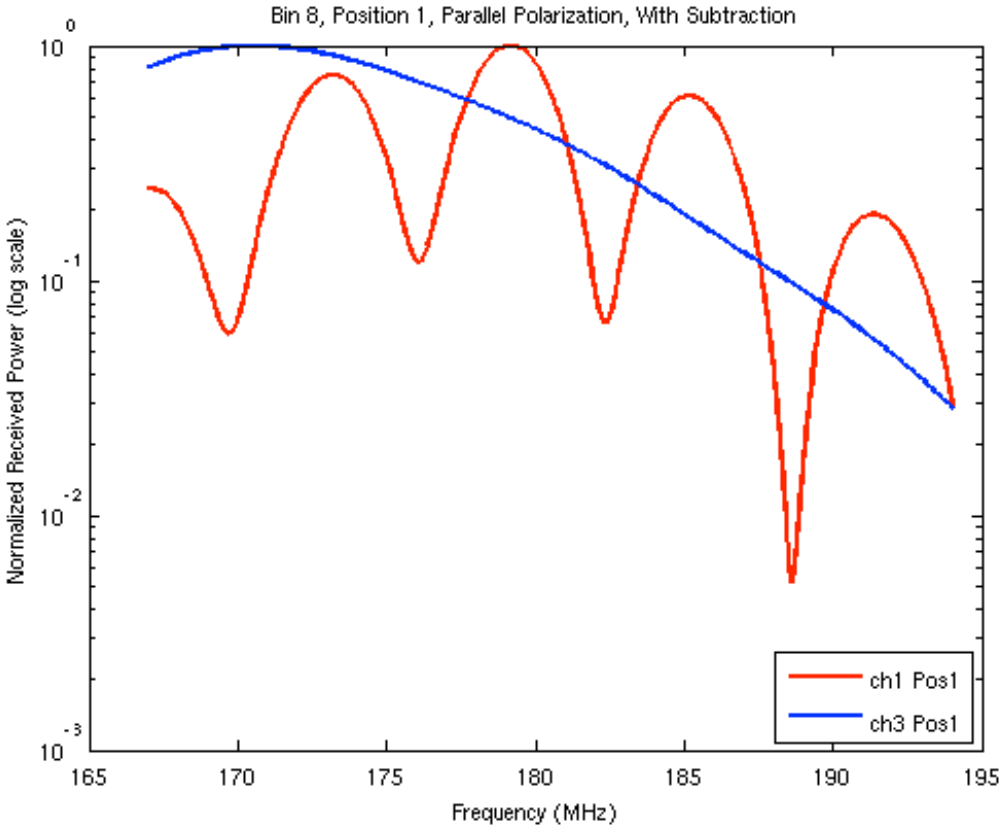

Figure 18: Frequency-domain signature of the cavern for Position 1 and for Bin 8.

The above figure signatures obtained with a shorter antenna, corresponding to Bin 8, but with more noticeable 6 MHZ separations in the peaks of Channel 1 (Corresponding to Figure 13, with the addition of Channel 3).

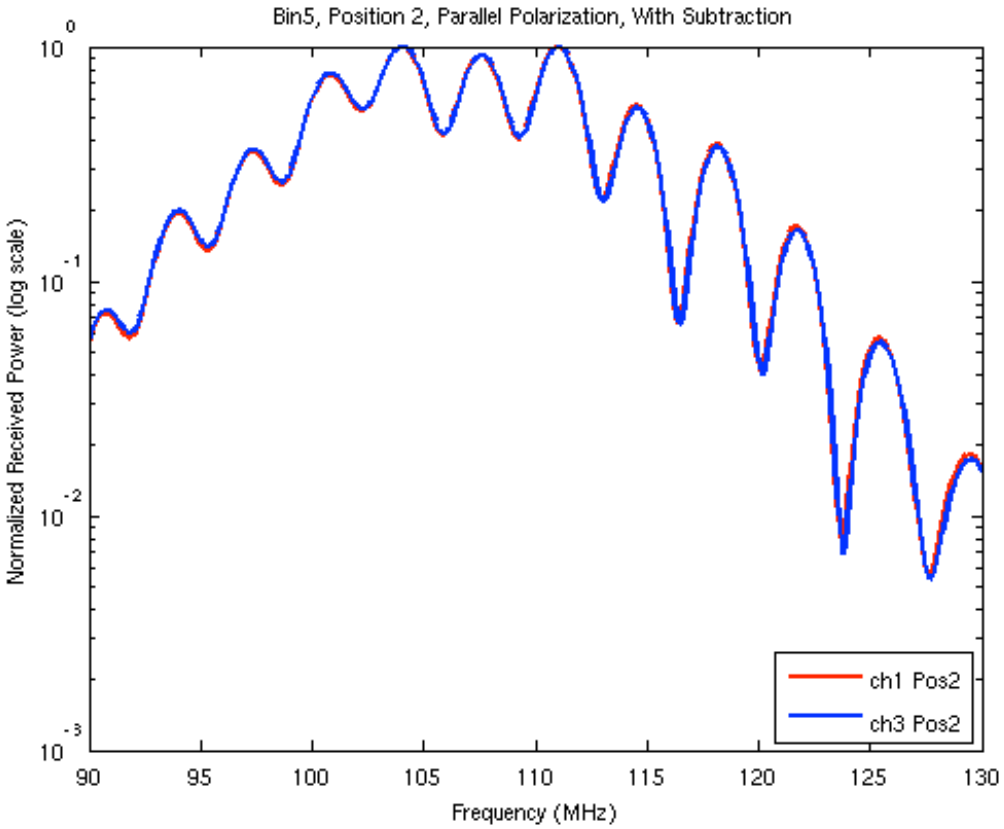

Figure 19: Frequency-domain signature of the cavern for Position 2.

In Figure 19, Channel 1 and Channel 2 overlap each other as expected due to symmetry with 3.5 MHz difference between peaks (Corresponding to Figure 12).

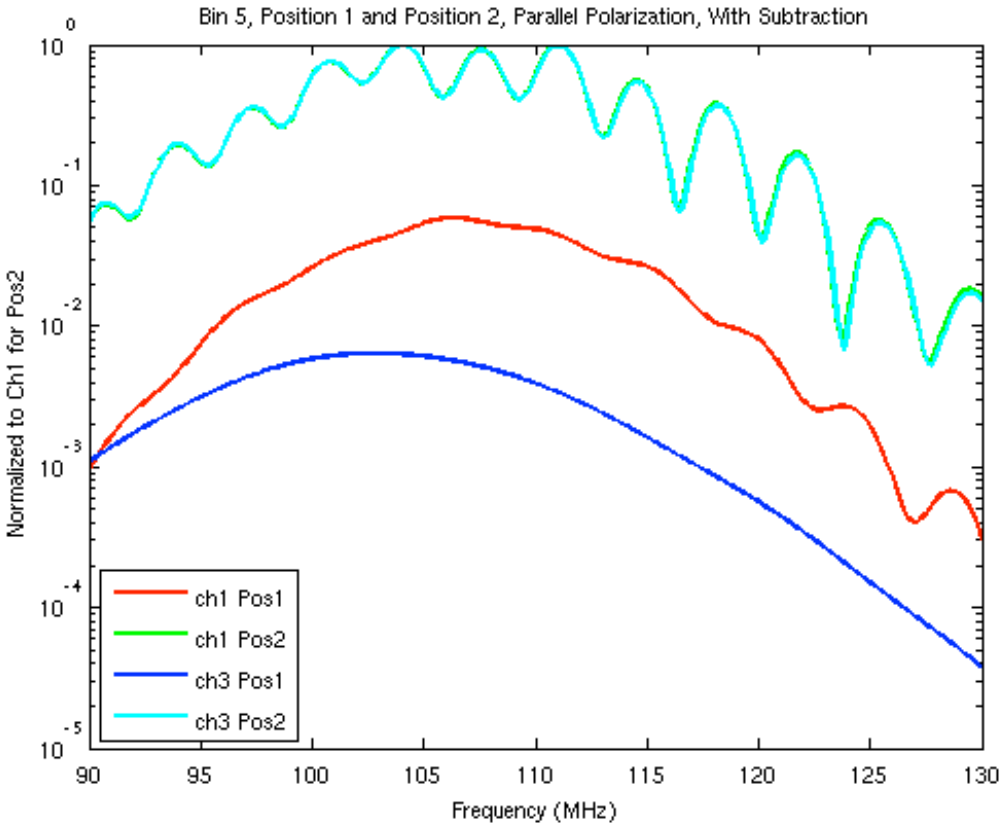

Figure 20: Frequency-domain signature of the cavern from Position 1 and Position 2.

The above figure combines Channel 1 and Channel 2 form Position 1 and Position 2, but normalize all with respect to the maximum obtained by channel 1 for position 2. For the position 2 channels, the receivers and source are too far away to pick up a clear cavern signature.

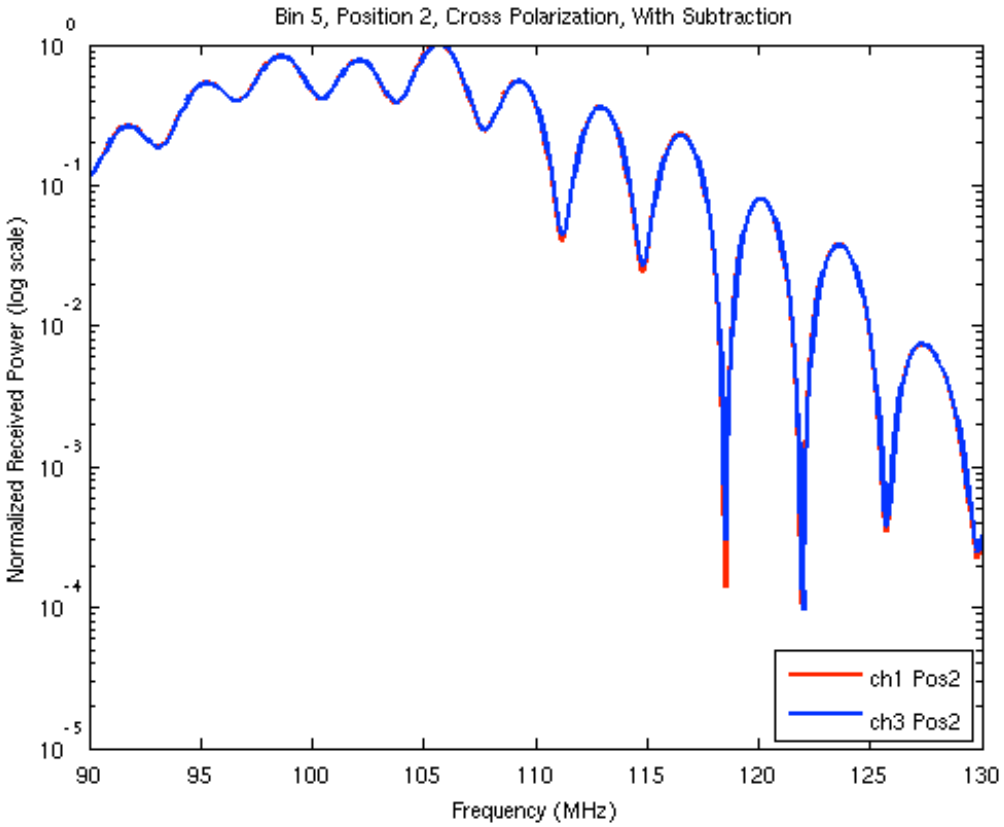

Figure 21: Frequency-domain signature of the cavern from Position 2 for the cross polarization case (Corresponding to Figure 14).

The above figure shows the case for cross polarization, which shows an approximate variation of 3.5 MHz between peaks for both channels.

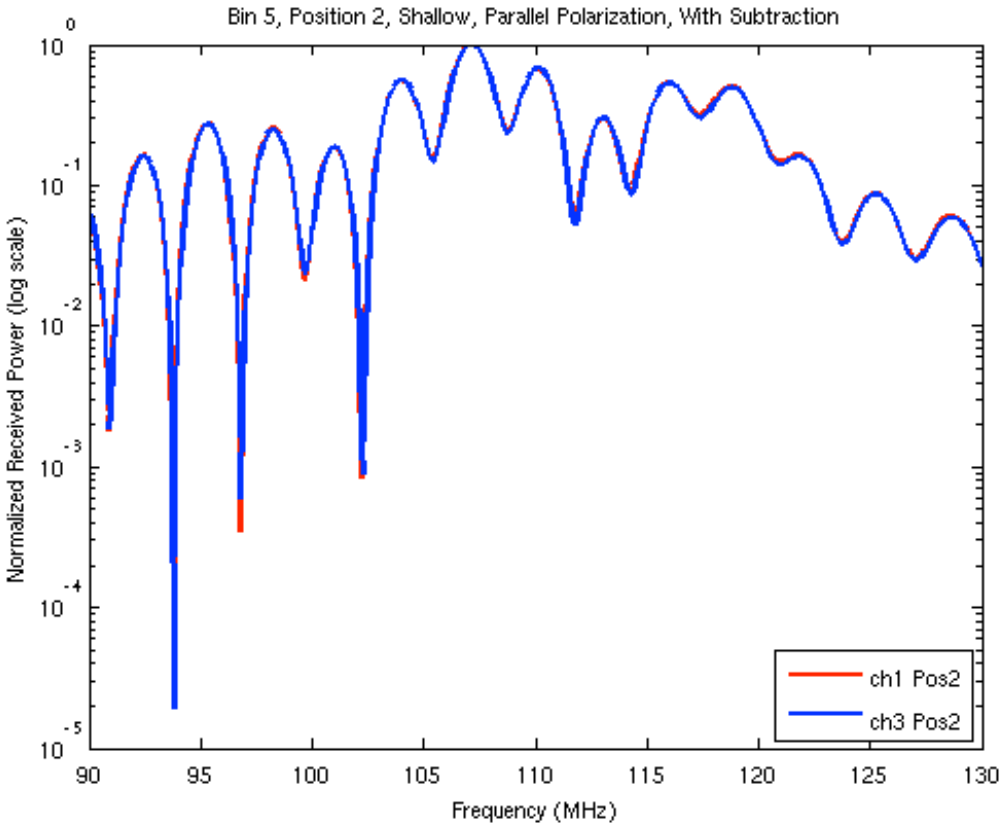

Figure 22: Frequency-domain signature of the cavern from Position 2 for a shallow cavern (Corresponding to *Figure 15*).

Figure 22 displays a 2.8 MHz difference between peaks for both channels.

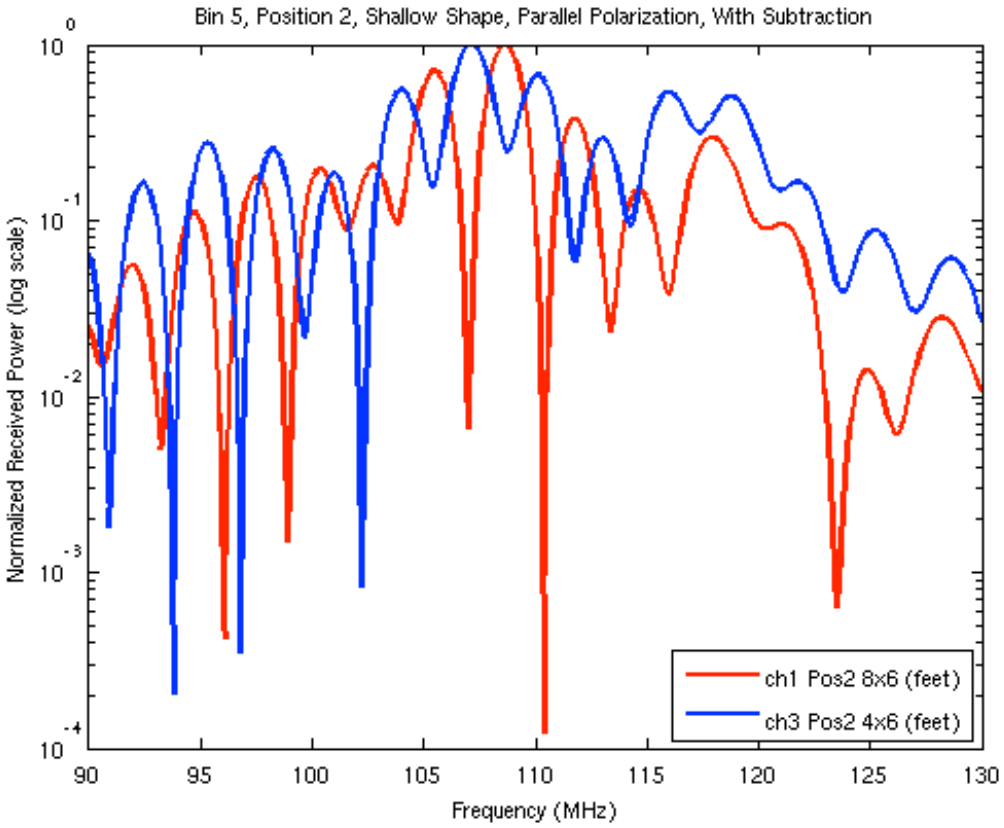

Figure 23: Frequency-domain signature of the cavern for Position 2, Channel 1, with the dimension of 4 X 6 feet. Position 2, Channel 1 shows the signature of a cavern with for a cavern of depth of 5 feet, but the dimensions of 8 x 6 feet (Corresponding to *Figure 16*).

6 Conclusion and Future Possibilities

This Thesis addressed the computational aspects of the remote detection and characterization of underground structures using the FDTD method. Specifically, tunnels located at China Lake, California were test structures. The tunnels varied in depth, and were situated in the earth's crust, composed of predominately granite. Several models investigated the signal received signal in both time and frequency domain to extract the signature of an air-filled cavern. To optimize the simulation, a CPML surrounded the computational domain to act as an absorbing boundary, and the source code utilized the MPI for parallel processing. Performing simulations provides a comprehensive and inexpensive solution to understanding various aspects of remote-sensing.

Just as previous work in this area provided a foundation for the remote-sensing study described in this Thesis, this research can be extended for future enhancements. The second phase of this research could encompass aerial surveys using a remote antenna. This scenario could be accomplished by implementing the Total-Field/Scattered-Field (TF/SF) in the existing FDTD models to simulate a plane wave incident on the ground and cavern as would be expected from a distant antenna on an aircraft. Implementing the TF/SF creates a special boundary inside of the FDTD grid. An advantage of using this technique is the ability to create a user defined angle of incidence for the impinging wave. This would provide a more realistic environment to model the detection of an underground structure from a moving aircraft. This additional

work could significantly advance the state-of-the-art of remote-sensing of underground caverns.

References

[1] A. Taflove and S. C. Hagness, Computational Electrodynamics: The Finite-Difference Time-Domain Method, Artech House: Norwood, MA, 2005.

[2] Message-Passing Interface (MPI), URL: www.mpi-forum.org

[3]URL: http://www.top500.org/list/2009/06/100

[4] L. L. Monte, D. Erricolo, F. Soldovieri, and M. C. Wicks, "Radio Frequency Tomography for Tunnel Detection", IEEE Transactions On Geoscience And Remote Sensing, Vol. 48, No. 3, March 2010

[5] D. M. Dobkin, The RF in RFID Passive UHF RFID in Practice, Library of Congress Cataloging-in-Publication Data, 2008

[6] T. Dogaru, and C. Le, "SAR Images of Rooms and Buildings Based on FDTD Computer Models", IEEE Transactions on Geoscience and Remote Sensing, Vol. 47, No. 5, May 2009

[7] D. Pena, R. Feick, H. Hristov, and W. Grote, "Measurement and modeling of propagation losses in brick and concrete walls for the 900-MHz band," IEEE Trans. Antennas Propag., vol. 51, no. 1, pp. 31–39, Jan. 2003.

[8] A. Muqaibel, A. Safaai-Jazi, A. Bayram, A. Attiya, and S. Riad, "Ultra-wideband through-the wall propagation," Proc. Inst. Elect. Eng.—Microw., Antennas Propag., vol. 152, no. 6, pp. 581–588, Dec. 2005

[9] W. Stone, "Electromagnetic signal attenuation in construction materials," Nat. Inst. Standards Technol., Gaithersburg, MD, NISTIR 6055, Oct. 1997.

[11] C. F. Yang, C. J. Ko, and B. C. Wu, "A free space approach for extracting the equivalent dielectric constants of the walls in buildings," in Proc. IEEE Antennas Propag. Int. Symp., Baltimore, MD, Jul. 1996, pp. 1036–1039

[9.] A. Taflove (1980). "Application of the finite-difference time-domain method to sinusoidal steady state electromagnetic penetration problems". *Electromagnetic Compatibility, IEEE Transactions on* **22**: 191–202

[11] Donohoe, J.P. Fairley, J. R. Lynch, "Locating Soil Anomalies Using the Impedance Variation of a Horizontal Dipole Over Ground", L.N. Antennas and Propagation Society International Symposium, 2009. APSURSI '09. IEEE

[12] P. Torrione and L. M. Collins, "Texture Features for Antitank Landmine Detection Using Ground Penetrating Radar," IEE Trans, Geoscience and Remote Sensing, Vol. 45, NO. 7, July 2007

[13] J. Sogade, Y. Vichabian, A. Vandiver, P. M. Reppert, D. Coles, and Frank Dale Morgan, “Electromagnetic Cave-to-Surface Mapping System”, IEEE Transactions On Geoscience And Remote Sensing, Vol. 42, No. 4, April 2004

[14] URL: http://en.wikipedia.org/wiki/Finite-difference_time-domain_method

[15] J.P. Berenger**, “**A perfectly matched layer for the absorption of electromagnetic waves”, Journal of Computational Physics, Volume 114, Issue 2, October 1994, Pages 185-200

[16] J.P. Berenger, “Improved PML for the FDTD solution of wave-structure interaction problems”, IEEE Trans Antennas Propagation 45 1997., 466-473.

[17] J.P. Berenger, “An effective PML for the absorption of evanes- cent waves in waveguides”, IEEE Microwave Guided Wave Lett 8 1998., 188-190.

[18] J.P. Berenger, “Evanescent waves in PML’s: Origin of the numeri- cal reflection in wave-structure interaction problems”, IEEE Trans Antennas Propagation 47 1999., 1497-1503.

[19] C. F. Austin and W. F. Durbin, “Mineral deposits and mineral potential of the Naval weapons center interrange access road corridor,” NWC TM 5340, May 1984.

Figures:

[1] URL: http://ab-initio.mit.edu/wiki/index.php/Image:Yee-cube.png